

Observation of carrier lifetime distribution in 4H-SiC thick epilayers using microscopic time-resolved free carrier absorption system

K. Nagaya¹, T. Hirayama¹, T. Tawara^{2,3}, K. Murata⁴, H. Tsuchida⁴, A. Miyasaka⁵,
K. Kojima³, T. Kato³, H. Okumura³, M. Kato^{1,6*}.

1. *Department of Electrical and Mechanical Engineering, Nagoya Institute of Technology, Nagoya 466-8555, Japan*

*E-mail: kato.masashi@nitech.ac.jp

2. *Fuji Electric Co., Ltd., 4-18-1 Tsukama, Matsumoto, Nagano 390-0821, Japan*

3. *National Institute of Advanced Industrial Science and Technology (AIST), 1-1-1 Umezono, Tsukuba, Ibaraki 305-8568, Japan*

4. *Central Research Institute of Electric Power Industry (CRIEPI), 2-6-1 Nagasaka, Yokosuka, Kanagawa 240-0196, Japan*

5. *SHOWA DENKO K.K., 1-13-9, Shibadaimon, Minato, Tokyo 105-0012, Japan*

6. *Frontier Research institute for Materials Science, Nagoya Institute of Technology, Nagoya 466-8555, Japan*

Abstract

The carrier lifetime is an important parameter for high voltage SiC bipolar devices because its distribution in drift layers affects the device performance. Observation techniques for carrier lifetime, along with the development of carrier lifetime control processes, are important to control carrier lifetime distribution. In this study, we developed a microscopic time-resolved free carrier absorption system that has a variable spot size of excitation light and two different probe light wavelengths (405 or 637 nm). By selecting a relatively small spot size of excitation light and the probe light of shorter wavelength (405 nm), the distribution of carrier lifetime was observed with a high spatial resolution of $\sim 3 \mu\text{m}$. Additionally, by using a relatively large spot size of excitation light and the probe light which leads to stronger free carrier absorption (637 nm), an accurate measurement of carrier lifetime was obtained. The developed system enables the design and development of bipolar SiC devices with carrier lifetime distribution control.

Introduction

Silicon carbide (SiC) is expected to be an attractive wide-bandgap semiconductor material for power device applications. Unipolar devices using SiC are commercially available and are widely employed in electric power conversion. However, the compatibility between the on-resistance and breakdown voltage of unipolar devices is limited.¹⁾ Meanwhile, bipolar devices can overcome this limitation owing to the effects of conductivity modulation, which employs both electrons and holes for electrical conduction. To induce the effects of conductivity modulation, the carrier lifetime in the drift layer must be sufficiently long. However, a long carrier lifetime enhances the reverse current during device switching. It is important to control the distribution of the carrier lifetime in the drift layer to achieve conductivity modulation effects with low switching reverse currents. In silicon bipolar devices, thin and short carrier lifetime layers have been frequently employed to achieve conductivity modulation with low switching currents.²⁾ For SiC, it has been suggested that the fabrication of a drift layer with carrier lifetime control can be achieved by combining carrier lifetime enhancement processes with a buried thin layer and vanadium (V) doping.³⁻⁶⁾

To control carrier lifetime distribution, developments in not only fabrication processes, but also observation techniques are important. Even if the device is designed for optimal carrier lifetime distribution, the distribution in the fabricated device will differ from the design. Therefore, a technique for measuring carrier lifetime with high spatial resolution must be developed to confirm the presence of thin and short carrier lifetime layers in the fabricated device. For SiC, three typical contactless techniques exist for carrier lifetime measurement: microwave photoconductivity decay (μ -PCD),⁷⁻¹⁷⁾ time-resolved photoluminescence (TR-PL)¹⁷⁻²²⁾, and time-resolved free carrier absorption (TR-FCA).^{17,23-35)} Among these techniques, TR-FCA uses probe and excitation lights, and measurements are performed on the area where both the lights overlap. Therefore, by focusing on either of the lights, a spatial resolution higher than those of μ -PCD and TR-PL can be achieved. Observation of the short carrier lifetime layer in silicon

has been reported by using TR-FCA.³⁵⁾ In addition, TR-FCA offers an advantage in the accurate evaluation of carrier lifetime under high-injection conditions.³⁴⁾

Here, we report the depth-resolved carrier lifetime measurements of 4H-SiC thick epilayers obtained using a microscopic TR-FCA system. By selecting the excitation laser spot size and the probe laser wavelength, we performed two modes of measurements to obtain either a high spatial resolution or an accurate estimate of carrier lifetime. From these measurements, we estimated the distribution of the carrier lifetime in thick epilayers with and without the PiN diode structure.

Experiments

Schematics of the sample structures are shown in Figs. 1(a)–(c). One of the samples has a PiN structure with a p⁺ contact layer, a p-type epilayer, an n-type drift layer, and an n⁺ buffer layer on an n-type 4H-SiC substrate. We named this sample PiN N dope, and it was fabricated by the following procedure. A 12 μm thick epilayer (n⁺ buffer layer) with an N doping concentration of $\sim 10^{18} \text{ cm}^{-3}$ was grown on the Si face of an n-type 4H-SiC 4° off-axis (0001) commercial substrate. Subsequently, a 150 μm thick n-type drift layer with an N doping concentration of $\sim 10^{14} \text{ cm}^{-3}$ was grown on the n⁺ buffer layer. A 2 μm p-type epilayer with an Al doping concentration of $\sim 10^{18} \text{ cm}^{-3}$ was grown on top of the n-type drift layer. The structure was subjected to thermal treatment (C-diffusion process) after the p-type epilayer growth to reduce the concentration of the recombination center, the Z_{1/2} center, in the drift layer. The structure was twice subjected to thermal oxidation at 1300 °C for 5 h. The oxide layer was etched off by hydrofluoric acid before the second thermal oxidation, followed by annealing at 1550 °C in Ar gas for 30 min.¹³⁾ The thermal treatment process was expected to reduce the thickness of the p-type epilayer by 200 nm. Then, a p⁺ contact layer was fabricated by Al ion implantation, forming a 0.3 μm thick box profile with an Al doping concentration of $\sim 10^{20} \text{ cm}^{-3}$ with post-implantation annealing at 1620 °C in Ar gas for 3 min. Another sample was fabricated with the same structure as that of the PiN N dope, except for a buried nitrogen and

vanadium (N/V) co-doped layer, which was formed by adding VCl_4 during its growth. Furthermore, the N/V co-doped layer had a V concentration of $\sim 10^{13} \text{ cm}^{-3}$ and a thickness of $11 \mu\text{m}$.⁶⁾ V doping was performed to reduce the carrier lifetime and resulted in a local short carrier lifetime layer. Such a structure reduces accumulated carriers and reverse currents during switching operations.⁵⁾ This sample was named PiN N/V co-dope. The sample was processed into a $1 \text{ mm} \times 3 \text{ mm}$ wide strip by mechanically grinding and polishing a $3 \text{ mm} \times 3 \text{ mm}$ chip from both the $(1\bar{1}00)$ and $(\bar{1}100)$ faces. Figure 1(c) shows another sample without any p-type layers. This sample has an epitaxial layer (thickness: $140 \mu\text{m}$) with a uniform N concentration ($\sim 10^{14} \text{ cm}^{-3}$) on the C-face of the 4H-SiC substrate. After epitaxial growth, the sample was subjected to C^+ implantation (total C^+ concentration: $\sim 10^{16} \text{ cm}^{-3}$) and annealing at $1650 \text{ }^\circ\text{C}$ for 5 min to enhance the carrier lifetimes.²⁰⁾ We named this sample N dope and the size of this sample was $3 \text{ mm} \times 20 \text{ mm}$. The cross section of the sample was treated by mechanically polishing the $(1\bar{1}00)$ and $(\bar{1}100)$ faces. We mechanically polished the $(1\bar{1}00)$ faces of all the samples prior to the measurements.

We employed a 355 nm pulsed yttrium aluminum garnet (YAG) laser as the excitation light with a pulse width of 1 ns and a repetition frequency of 100 Hz. The injected photon density was set at 10^{16} cm^{-2} , which corresponds to an average excess carrier density of $1.5 \times 10^{18} \text{ cm}^{-3}$ up to the penetration depth ($\sim 42 \mu\text{m}$). A continuous wave laser of wavelength 405 or 637 nm was used as a probe light for the microscopic TR-FCA system. The probe light with 405 nm wavelength enabled measurements at high spatial resolutions as it is almost the shortest wavelength below the band gap energy of 4H-SiC. Further, the probe light of 637 nm wavelength has a higher free carrier absorption peak than the 405 nm probe light, which enabled the achievement of a high signal-to-noise ratio.^{30,36)} The sample was illuminated by the excitation and probe lights through an objective lens with a numerical aperture (NA) of 0.65. The spot diameter of the probe light at the focal point was $\sim 1 \mu\text{m}$, whereas the spot size of the excitation light could be modified using a variable aperture and a convex lens in front of the objective lens. The probe light, which is transmitted from the $(1\bar{1}00)$ face to the $(\bar{1}100)$ face of the sample, was detected using a silicon

photodiode (Si-PD). A long-pass filter (LPF) to block light of 355 nm wavelength and a bandpass filter (BPF) to pass the probe light of 405 nm or 637 nm wavelength were placed in front of the Si-PD. During the measurement, the sample was moved along the depth direction with respect to the objective lens by using a stepper motor. The step size was selected to restrict the total measurement time to several hours. Figure 2 shows a schematic of our microscopic TR-FCA system. All the measurements were performed at room temperature.

We defined two measurement modes: fine and expanded measurements. In the fine measurement mode, the excitation light was focused to a spot diameter of $\sim 30 \mu\text{m}$ on the sample, and the probe light of 405 nm wavelength was selected. This mode enabled measurements with a high spatial resolution. In the expanded measurement mode, the excitation light was focused to a spot diameter of $\sim 90 \mu\text{m}$ on the sample, and the probe light of 637 nm wavelength was selected. This mode enabled the accurate evaluation of carrier lifetimes with moderate spatial resolution. The expected optical paths for the fine and expanded measurement modes are shown in Figs. 3(a) and 3(b), respectively, using refractive indices of 2.83, 2.75, and 2.63 for 355, 405, and 637 nm lights, respectively.³⁷⁾ As shown in this figure, the probe light expanded from the $(1\bar{1}00)$ surface of the sample, resulting in a wider measurement region than the spot diameter of $\sim 1 \mu\text{m}$. In the fine measurement mode, the region of overlap of the excitation light and probe light has a maximum radius of $7.8 \mu\text{m}$ at a depth of $36.5 \mu\text{m}$ and a radius of $6.8 \mu\text{m}$ at the penetration depth of the excitation light ($42 \mu\text{m}$). The excited carrier concentration was the highest at the $(1\bar{1}00)$ face and gradually decreased with increasing depth. Therefore, most of the signals originate from a radius of a few microns around the probe light spot. With time, the carriers recombine and diffuse out of the path of the probe light, and thus the decay of the signal includes both recombination and diffusion. In the expanded measurement mode, the region of overlap has a maximum radius of $23.6 \mu\text{m}$ at a depth of $109 \mu\text{m}$ and a radius of $9.4 \mu\text{m}$ at $42 \mu\text{m}$ depth. Therefore, the signals originate from a radius of $\sim 10 \mu\text{m}$ around the

probe light spot. In this case, the excited carriers are distributed within a diameter of $90\ \mu\text{m}$ at the $(1\bar{1}00)$ face, and this wide carrier distribution suppresses the carrier diffusion in the $\langle 0001 \rangle$ and $\langle 11\bar{2}0 \rangle$ directions. Thus, the decay of the signal predominantly depends on the carrier recombination.

Results and Discussion

Figure 4 shows the depth-resolved TR-FCA decay curves of the (a) PiN N dope, (b) PiN N/V co-dope, and (c) N dope samples, obtained by fine measurement. For all the figures, we defined $X = 0\ \mu\text{m}$ at the top of the samples (for PiN N dope and PiN N/V co-dope, which is the surface of the p-type layer). The decay curves of the PiN N dope sample were almost uniform in the depth direction, whereas fast decay curves were observed from 10 to $35\ \mu\text{m}$ depth in the PiN N/V co-dope sample. Meanwhile, N dope showed slower decay curves near the (0001) surface than that of the other samples. To observe the distributions of the carrier lifetimes, we defined the $1/e$ lifetime as the time for the TR-FCA signal decay from a peak to $1/e$ of the peak.

Figure 5(a) shows the secondary ion mass spectrometry (SIMS) profile of V concentrations of the PiN N/V co-dope sample. The $11\ \mu\text{m}$ thick N/V co-doped layer was located at a depth of $22\ \mu\text{m}$ from the (0001) surface. Figure 5(b) shows the depth distributions of $1/e$ lifetimes at $2.5\ \mu\text{m}$ intervals in the PiN N dope and PiN N/V co-dope samples, and the inset shows the measurement at $0.5\ \mu\text{m}$ intervals of X from $20\text{--}35\ \mu\text{m}$. The $1/e$ lifetimes of the PiN N dope sample were uniform in the n-type drift layer, whereas the PiN N/V co-dope sample showed a local $1/e$ lifetime reduction at $20\text{--}35\ \mu\text{m}$ from the surface, which corresponded to the depth of the N/V co-doped layer. As shown in the inset of Fig. 5(b), we observed a sharp reduction in the $1/e$ lifetime at $31\text{--}34\ \mu\text{m}$, which is the edge of the N/V co-doped layer. This indicates that the spatial resolution of the fine measurement is $\sim 3\ \mu\text{m}$, which is almost the same as the average radius of the probed region shown in Fig. 3(a). The achieved resolution was similar to or even better than

the reported FCA results owing to the use of the high NA objective lens and the short wavelength of the probe light.²⁴⁾ The $1/e$ lifetimes within the N/V co-doped layer were not uniform and did not correspond to the V distribution measured by SIMS. The origins of these nonuniform $1/e$ lifetimes within the N/V co-doped layer are unclear. However, the V concentration measured by SIMS is near the SIMS detection limit, and a nonuniform V distribution may exist within the N/V co-doped layer. Figure 5(c) shows the depth distribution of $1/e$ lifetime at $1\ \mu\text{m}$ intervals in the N dope sample, obtained by fine measurements. Relatively long $1/e$ lifetimes were observed at X of $80\text{--}120\ \mu\text{m}$ compared with other regions, even though the epilayer had a uniform doping concentration ($\sim 10^{14}\ \text{cm}^{-3}$) in the depth direction. This result indicates that even if an epilayer is grown in a consistent condition, the carrier lifetime will vary within the epilayer. The origin of this variation should be investigated further. The $1/e$ lifetimes obtained from the fine measurements for all the samples were short compared with previously reported carrier lifetimes for the epilayer after carrier lifetime enhancement processes.^{13-15,19-21)} Though this measurement mode offers high spatial resolution, it is difficult to accurately evaluate the carrier lifetimes.

Figure 6 shows the depth-resolved TR-FCA decay curves of the (a) PiN N dope, (b) PiN N/V co-dope, and (c) N dope samples, obtained from the expanded measurements. For all the samples, the decays obtained by the expanded measurement were found to be slower than those obtained by the fine measurements (Fig. 4).

Figure 7(a) shows the depth distributions of the $1/e$ lifetimes at $2.5\ \mu\text{m}$ intervals in the PiN N dope and PiN N/V co-dope samples, obtained by the expanded measurements, and the inset shows the $1/e$ lifetime distribution of both samples at $0.5\ \mu\text{m}$ intervals around the N/V co-doped layer. The $1/e$ lifetimes obtained from expanded measurements were longer than those obtained by the fine measurements (Fig. 5(b)). Although a local lifetime reduction by the N/V co-doped layer was observed, the reduction was more gradual than that observed by the fine measurements. The reduction in the $1/e$ lifetime at the edge of the

N/V co-doped layer is shown in the inset figure. This indicates that the expanded measurements had a lower spatial resolution ($13\ \mu\text{m}$) than that of the fine measurements (Fig. 5(b)).

Figure 7(b) shows the depth distributions of the $1/e$ lifetimes in the N dope sample, obtained by the expanded measurement. For estimating the bulk high injection lifetime by the calculations described later, we present the $1/e^2$ and $1/e^3$ lifetimes, which are defined as decay times from $1/e$ to $1/e^2$ and from $1/e^2$ to $1/e^3$, respectively.²¹⁾ The $1/e$ lifetimes obtained by the expanded measurements were longer than those obtained by the fine measurements (Fig. 5(c)). The $1/e^2$ and $1/e^3$ lifetimes were slightly longer near the substrate compared to that near the surface, similar to the pattern of the $1/e$ lifetime distribution in Fig. 5(c). In addition, the values of the $1/e$ lifetimes in the N dope sample were ~ 10 times longer than those in the PiN N dope and the PiN N/V co-dope samples. The longer lifetimes in the N dope sample can have three possible origins : (i) the difference in growth conditions induced a low $Z_{1/2}$ center concentration for N dope, (ii) the ion implantation and post-implantation annealing processes for the p^+ contact layers for PiN N dope and PiN N/V co-dope induced defects in the drift layers, and (iii) the lifetime enhancement process was only effective before the p-type layer was formed; however, for PiN N dope and PiN N/V co-dope, the process was performed after the p-type layer formation.³⁸⁾ When we grew an epilayer with a single n-type layer, we obtained a long lifetime in the layer after the lifetime enhancement process. Hence, origin (i) is unlikely. For origin (ii), because the temperature (1620°C) of the post-implantation annealing was low enough to prevent significant $Z_{1/2}$ center generation,³⁹⁻⁴¹⁾ a possible origin of the short carrier lifetime was defects formed by the ion implantation. Such the defects should result in a short lifetime near the ion implanted layer, while the results in Fig. 5(b) show a short lifetime within the entire epilayer. Hence, origin (ii) is also not possible, and thus origin (iii) is the most plausible explanation of the longer lifetime in the N dope sample. The detailed mechanism of origin (iii) is not clear and will be investigated in our future studies.

To confirm the bulk lifetime of the N dope sample, we calculated the excess carrier decay at each depth position inside the epilayer using the partial differential equation of excess carrier density as follows:

$$\frac{\partial n}{\partial t} = D \frac{\partial^2 n}{\partial X^2} - \frac{n}{\tau_{HL}} - Bn^2 - Cn^3 + G, \quad (1),$$

where n is the excess carrier density, D is the ambipolar diffusion coefficient, τ_{HL} is the high-injection lifetime, B is the radiative bimolecular recombination coefficient, C is the Auger recombination coefficient, and G is the generation rate of the carrier, which is negligible after the initial excitation. We employed electron and hole mobilities to obtain D as in Ref. 10 and adopted the reported values for B and C , i.e., 2×10^{-14} and 5×10^{-31} cm⁶/s, respectively.^{10,31,42)} Although the actual excess carriers diffused three-dimensionally after the excitation, for simplicity, we solved this equation in the depth direction (in the X direction, as shown Fig. 1(c)). We also assumed a constant τ_{HL} throughout the epilayer. The boundary conditions are expressed as follows:

$$D \frac{\partial n}{\partial X} \Big|_{X=0} = S_1 n \text{ and } D \frac{\partial n}{\partial X} \Big|_{X=140} = -S_2 n, \quad (2),$$

where S_1 and S_2 are the recombination velocities at the surface ($X = 0$) and the epilayer/substrate interface ($X = 140$), respectively. We assumed a surface and interface recombination of 1000 cm/s.^{7-10, 15, 28)} In the excess carrier decay model, n and τ_{HL} were parameters for fitting the measured depth distributions of the lifetimes. We obtained the parameters that minimized the residual sum of squares of the relative error between the measured and calculated $1/e$, $1/e^2$, and $1/e^3$ lifetime distributions. The lines in Fig. 6(b) show the calculated results with the minimum error for $n = 3.0 \times 10^{18}$ cm⁻³ and τ_{HL} of 10 μ s. The n of 3.0×10^{18} cm⁻³ was slightly larger than the measurement condition of 1.5×10^{18} cm⁻³, and the calculated $1/e$ lifetimes showed relatively large differences from the experiments compared with the $1/e^2$ and $1/e^3$ lifetimes. We assumed that these differences were due to not considering the surface recombination at the excited surface

in the calculation and the difference between B and C from the actual values. B and C depend on the doping concentrations^{28,31,42,43}, and our sample had a lower doping concentration than those employed in previous studies. However, the reported τ_{HL} for the sample from the same wafer as our sample was 11.4 μs , as estimated by $\mu\text{-PCD}$, which is close to our estimated value of 10 μs . Hence, the expanded measurements reflected the accurate carrier lifetimes in the epilayer bulk.¹⁴⁾ Therefore, we were able to observe the fine distribution of the carrier lifetimes by the fine measurements and accurately evaluate carrier lifetimes by the expanded measurements.

Conclusions

We performed depth-resolved measurements of carrier lifetimes in thick SiC epilayers using a microscopic TR-FCA system with variable spot sizes of excitation light and two different probe lights. Using the fine measurement mode, which has a spatial resolution of $\sim 3 \mu\text{m}$ and employed a small spot size of excitation light and a short probe light wavelength, we observed the difference between samples with and without a 11 μm thick short carrier lifetime layer. Further, from the expanded measurements, which employed a large spot size of excitation light and a probe light with strong free carrier absorption, the τ_{HL} was estimated to be 10 μs for the lifetime enhanced sample, which was close to the value obtained by the $\mu\text{-PCD}$ measurements. Therefore, the selection of the optimum excitation light spot size and probe light wavelength in the microscopic TR-FCA measurements yielded carrier lifetime distribution measurements with high spatial resolutions and accurate carrier lifetimes. These results demonstrate the usefulness of our microscopic TR-FCA system for observing the carrier lifetime distribution in SiC epilayers and its potential for accelerating the development of bipolar SiC devices.

Acknowledgments

This work is supported by the Strategic Innovation Promotion Program (SIP) of the Council for Science, Technology, and Innovation [Next Generation Power Electronics / Integrated Research and Development of SiC for next-generation power electronics] (management corporation: NEDO) and is partly supported by JST VP29117938885. The last author also thanks K. Muto of Mutsumi Corporation for his help in the development of the measurement system.

Data availability

The data that support the findings of this study are available from the corresponding author upon reasonable request.

References

- 1) T. Kimoto, Jpn. J. Appl. Phys. **58**, 018002 (2019).
- 2) M. Saggio, V. Raineri, R. Letor, and F. Frisina, IEEE Electron Device Lett. **18**, 333 (1997).
- 3) H. Tsuchida, I. Kamata, T. Miyazawa, M. Ito, X. Zhang, and M. Nagano, Mater. Sci. Semicond. Process. **78**, 2 (2018).
- 4) T. Miyazawa, T. Tawara, R. Takanashi, and H. Tsuchida, Appl. Phys. Express **9**, 111301 (2016).
- 5) K. Nakayama, T. Hatakeyama, Y. Yonezawa, H. Okumura, and H. Tsuchida, Extended Abstract of ICSCRM2017, TH.D1.9.
- 6) K. Murata, T. Tawara, A. Yang, R. Takanashi, T. Miyazawa, and H. Tsuchida, J. Appl. Phys. **126**, 045711 (2019).
- 7) M. Kato, A. Yoshida, and M. Ichimura, Jpn. J. Appl. Phys. **51**, 02BP12 (2012).
- 8) Y. Mori, M. Kato, and M. Ichimura, J. Phys. D Appl. Phys. **47**, 335102 (2014).
- 9) Y. Ichikawa, M. Ichimura, T. Kimoto, and M. Kato, ECS J. Solid State Sci. Technol. **7**, Q127 (2018).
- 10) M. Kato, Z. Xinchu, K. Kohama, S. Fukaya, and M. Ichimura, J. Appl. Phys. **127**, 195702 (2020).
- 11) T. Kimoto, K. Danno, and Jun Suda, Phys. Status Solidi B **245**, 1327 (2008).
- 12) T. Kimoto, Y. Nanen, T. Hyashi, and J. Suda, Appl. Phys. Express. **3**, 121201 (2010).
- 13) T. Kimoto, T. Hiyoshi, T. Hayashi, and J. Suda, J. Appl. Phys. **108**, 083721 (2010).
- 14) M. Kushibe, J. Nishio, R. Iijima, A. Miyasaka, H. Asamizu, H. Kitai, R. Kosugi, S. Harada, and K. Kojima, Mater. Sci. Forum **432-435**, 924 (2018).
- 15) S. Ichikawa, K. Kawahara, J. Suda, and T. Kimoto, Appl. Phys. Express **5**, 101301 (2012).
- 16) T. Tawara, H. Tsuchida, S. Izumi, I. Kamata, and K. Izumi, Mater. Sci. Forum **457-460**, 565 (2004).
- 17) P. B. Klein, J. Appl. Phys. **103**, 033702 (2008).

- 18) P. B. Klein, B. V. Shanabrook, S. W. Huh, A. Y. Polyakov, M. Skowronski, J. J. Sumakeris, and M. J. O'Loughlin, *Appl Phys. Lett.* **88**, 052110 (2006).
- 19) T. Miyazawa, and H. Tsuchida, *J. Appl. Phys.* **113**, 083714 (2013).
- 20) L. Storasta, and H. Tsuchida, *Appl. Phys. Lett.* **90**, 062116 (2007).
- 21) T. Miyazawa, M. Ito, and H. Tsuchida, *Appl. Phys. Lett.* **97**, 202106 (2010).
- 22) P. B. Klein, A. Shrivastava, and T. S. Sudarshan, *Phys. Status Solidi A* **208**, 2790 (2011).
- 23) P. Ščajev, V. Gudelis, K. Jarašiūnas, and P. B. Klein, *J. Appl. Phys.* **108**, 023705 (2010).
- 24) V. Grivickas, A. Galeckas, V. Bikbajevs, J. Linnros, and J.A. Tellefsen, *Thin. Solid. Films.* **364**, 181 (2000).
- 25) A. Galeckas, J. Linnros, V. Grivickas, U. Lindefelt, and C. Hallin, *Appl. Phys. Lett.* **71**, 3269 (1997).
- 26) S.S. Suvanam, K. Gulbinas, M. Usman, M.K. Lin- nerson, D.M. Martin, J. Linnros, V. Grivickas, and A. Hallén, *J. Appl. Phys.* **117**, 105309 (2015).
- 27) J. Linnros, *Appl. Phys. Lett.* **84**, 275 (1998).
- 28) A. Galeckas, V. Grivickas, J. Linnros, H. Bleichner, and C. Hallin, *Appl. Phys. Lett.* **81**, 3522 (1997).
- 29) S. Mae, T. Tawara, H. Tsuchida, and M. Kato, *Mater. Sci. Forum* **924**, 269 (2018).
- 30) P. Grivickas, K. Redeckas, K. Gulbinas, A. M. Conway, L. F. Voss, M. Bora, S. Sampayan, M. Vengris, and V. Grivickas, *J. Appl. Phys.* **125**, 225701 (2019).
- 31) P. Ščajev and K. Jarašiūnas, *J. Phys. D: Appl. Phys.* **46**, 265304 (2013).
- 32) A. Galeckas, J. Linnros, M. Frischholz, and V. Grivickas, *Appl. Phys. Lett.* **79**, 365 (2001).
- 33) P. Grivickas, J. Linnros, and V. Grivickas, *J. Mater. Res.* **16**, 524 (2001).
- 34) L. Subačius, K. Jarašiūnas, P. Ščajev, and M. Kato, *Meas. Sci. Technol.* **26**, 125014 (2015).
- 35) J. Linnros, P. Norlin, and A. Hallen, *IEEE Trans. Electron Devices* **40**, 2065 (1993).

This is the author's peer reviewed, accepted manuscript. However, the online version of record will be different from this version once it has been copyedited and typeset.
PLEASE CITE THIS ARTICLE AS DOI: 10.1063/1.50015199

- 36) S. Limpijumng, W. Lambrecht, S. Rashkeev, and B. Segall, Phys. Rev. B **59**, 12890 (1999).
- 37) S. Zollner, J.G. Chen, E. Duda, T. Wetteroth, S.R. Wilson, and J.N. Hilfiker, J. Appl. Phys. **85**, 8353 (1999).
- 38) N. Kaji, H. Niwa, J. Suda, and T. Kimoto, IEEE Trans. Electron Devices **62**, 374 (2015).
- 39) B. Zippelius, J. Suda, and T. Kimoto, J. Appl. Phys. **111**, 033515 (2012).
- 40) E. Saito, J. Suda, and T. Kimoto, Appl. Phys. Express **9**, 061303 (2016).
- 41) H.M. Ayedh, R. Nipoti, A. Hallén, and B.G. Svensson, J. Appl. Phys. **122**, 025701 (2017).
- 42) K. Neimontas, T. Malinauskas, R. Aleksiejūnas, M. Sudžius, K. Jarašiūnas, L. Storasta, J. P. Bergman, and E. Janzen, Semicond. Sci. Technol. **21**, 952 (2006).
- 43) T. Tawara, T. Miyazawa, M. Ryo, M. Miyazato, T. Fujimoto, K. Takenaka, S. Matsunaga, M. Miyajima, A. Otsuki, Y. Yonezawa, T. Kato, H. Okumura, T. Kimoto, and H. Tsuchida, J. Appl. Phys. **120**, 115101 (2016).

Figure captions

Fig. 1. Schematics of the sample structures. (a) PiN N dope has a PiN structure with a p^+ layer, a p-type epilayer, an n-type drift layer, and an n^+ buffer layer on the Si-face of a 4H-SiC substrate. (b) PiN N/V co-dope has the same structure as that of the PiN N dope, except for a buried N/V co-doped layer. (c) N dope has an epitaxial layer on the C-face of the 4H-SiC substrate.

Fig. 2. Schematic of the microscopic TR-FCA system. The spot diameter of the excitation light can be modified by the aperture size. One of the two probe lights of 405 nm or 637 nm wavelengths can be selected during the measurement.

Fig. 3. Expected optical paths for the (a) fine and (b) expanded measurement modes.

Fig. 4. Depth-resolved TR-FCA decay curves of the (a) PiN N dope, (b) PiN N/V co-dope, and (c) N dope samples, obtained by fine measurements.

Fig. 5. (a) SIMS profile of V concentration of the PiN N/V co-dope sample. (b) Depth distributions of $1/e$ lifetimes in the PiN N dope and PiN N/V co-dope samples, obtained by fine measurement. The inset is the measurement of the $1/e$ lifetime at $0.5 \mu\text{m}$ intervals around the N/V co-doped layer. (c) Depth distribution of $1/e$ lifetime in the N dope sample, obtained by fine measurement.

Fig. 6. Depth-resolved TR-FCA decay curves of the (a) PiN N dope, (b) PiN N/V co-dope, and (c) N dope samples, obtained by expanded measurements.

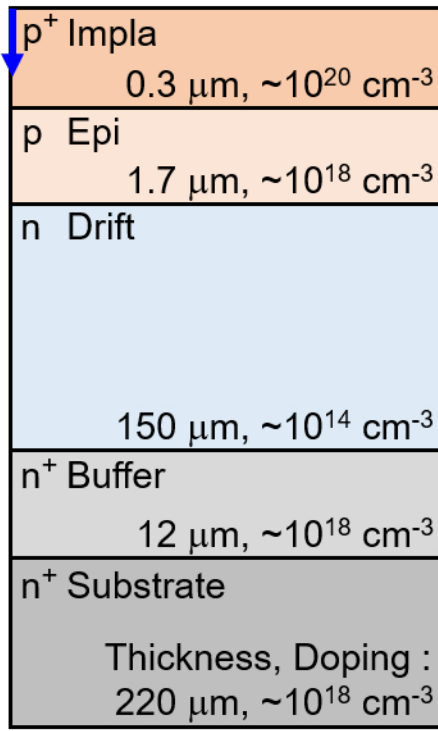
This is the author's peer reviewed, accepted manuscript. However, the online version of record will be different from this version once it has been copyedited and typeset.

PLEASE CITE THIS ARTICLE AS DOI: 10.1063/5.0015199

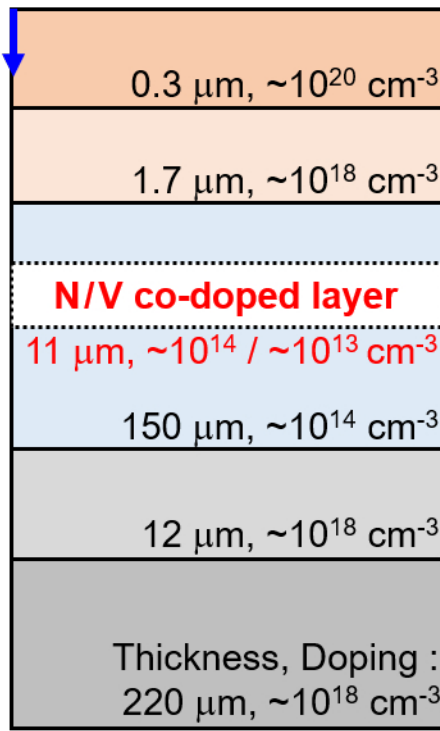
Fig. 7. (a) Depth distribution of $1/e$ lifetime in the PiN N dope and PiN N/V co-dope samples, obtained by expanded measurements. The inset is the distribution measured at $0.5 \mu\text{m}$ intervals around an N/V co-doped layer. (b) Lifetime distribution, measured by expanded measurement and the calculated results, of the N dope sample.

This is the author's peer reviewed, accepted manuscript. However, the online version of record will be different from this version once it has been copyedited and typeset. PLEASE CITE THIS ARTICLE AS DOI: 10.1063/5.0015199

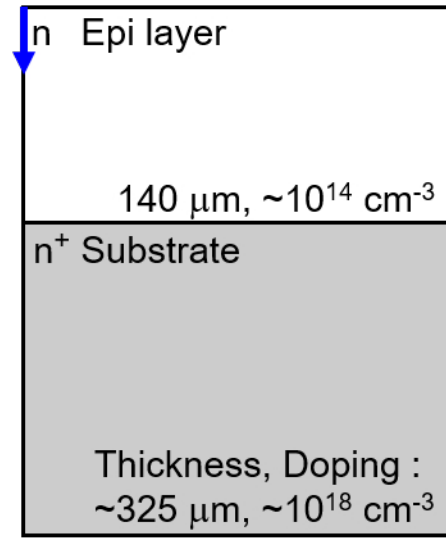
(a) PiN N dope



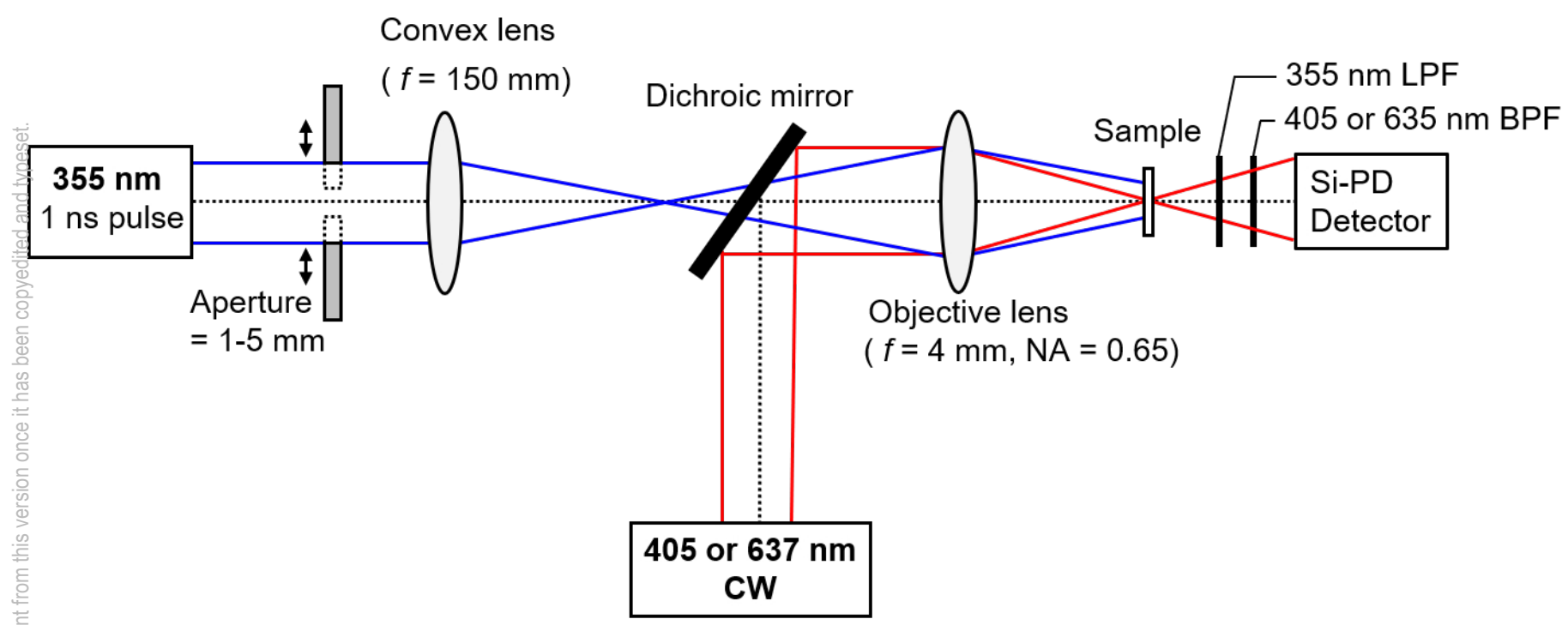
(b) PiN N/V co-dope



(c) N dope

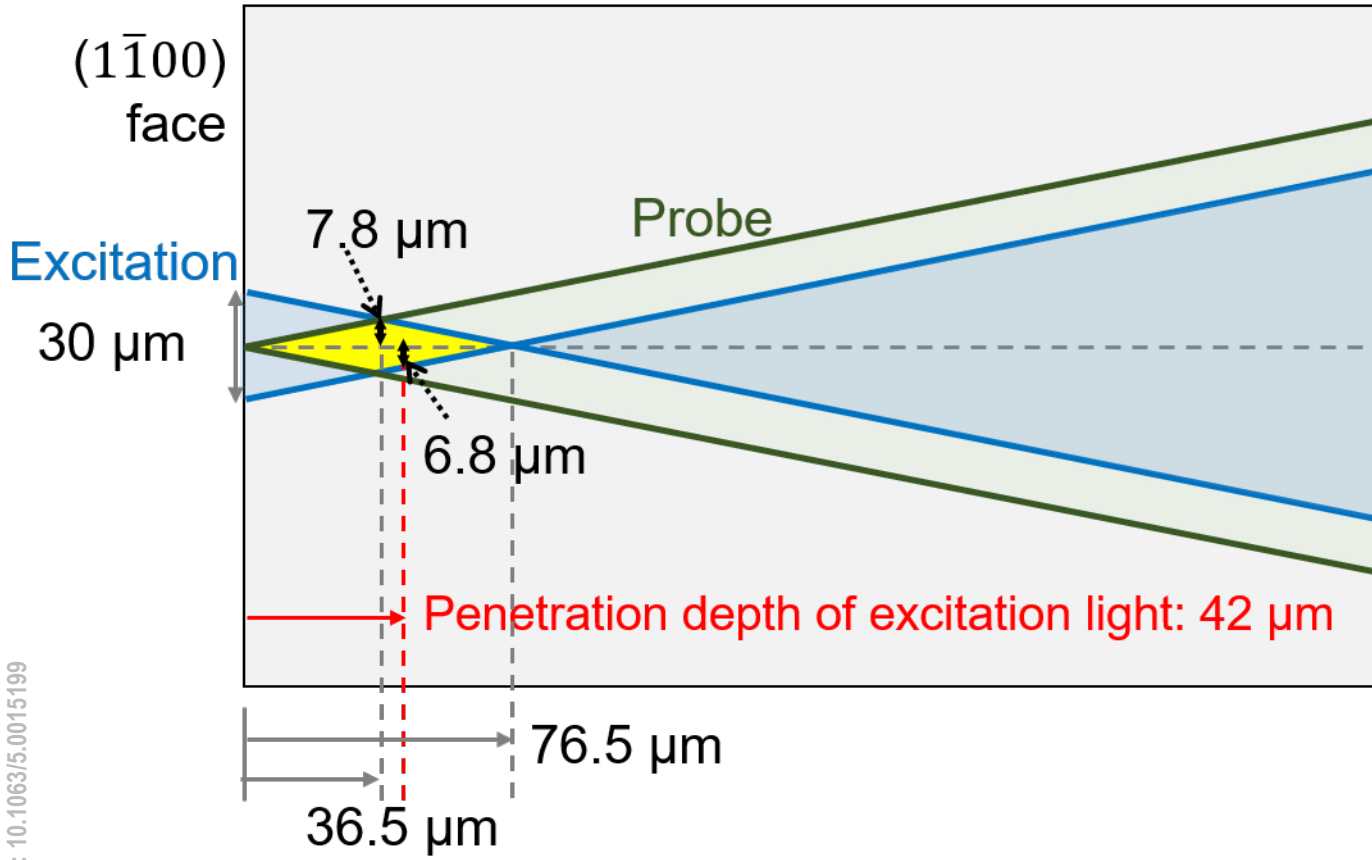


This is the author's peer reviewed, accepted manuscript. However, the online version of record will be different from this version once it has been copyedited and typeset.
PLEASE CITE THIS ARTICLE AS DOI: 10.1063/5.0015199

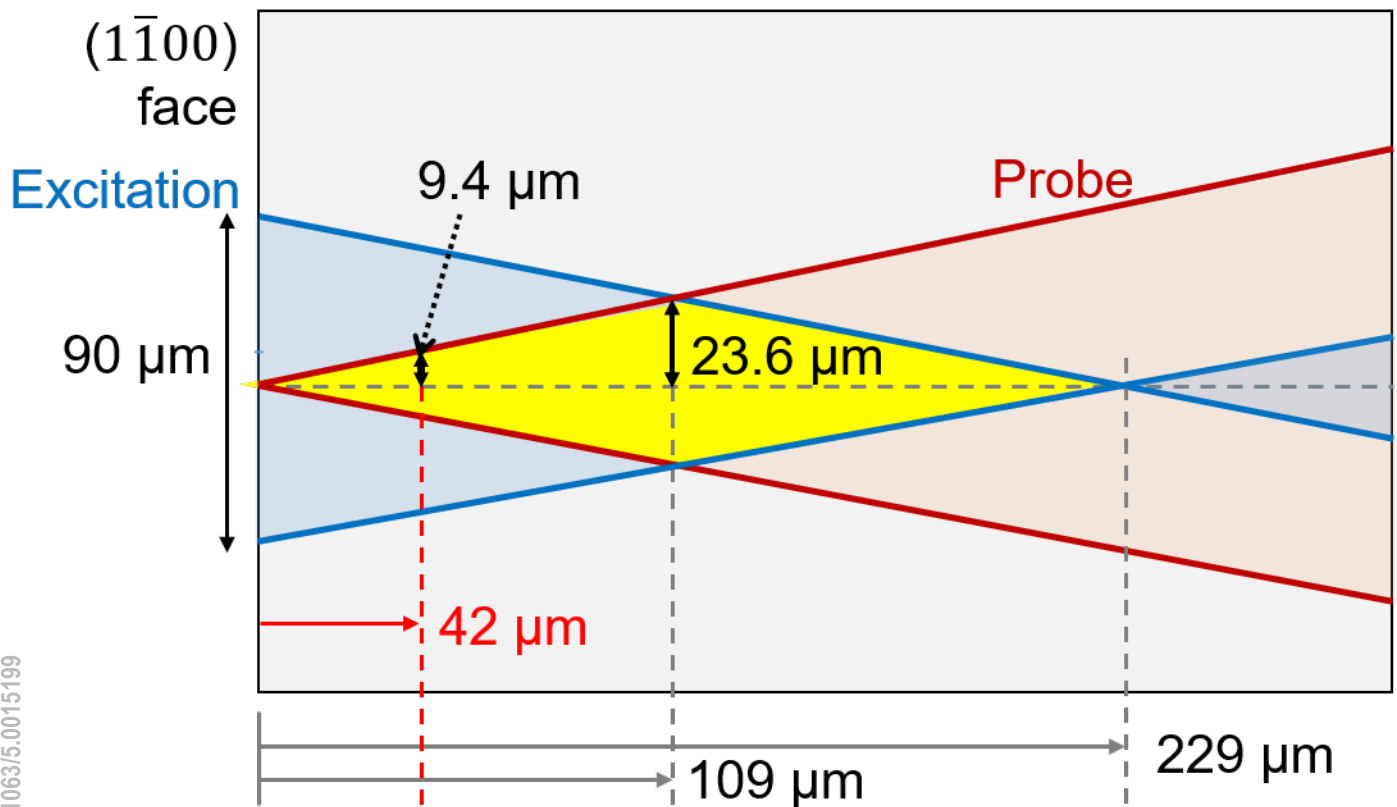


This is the author's peer reviewed, accepted manuscript. However, the online version of record will be different from this version once it has been copyedited and typeset.
PLEASE CITE THIS ARTICLE AS DOI: 10.1063/5.0015199

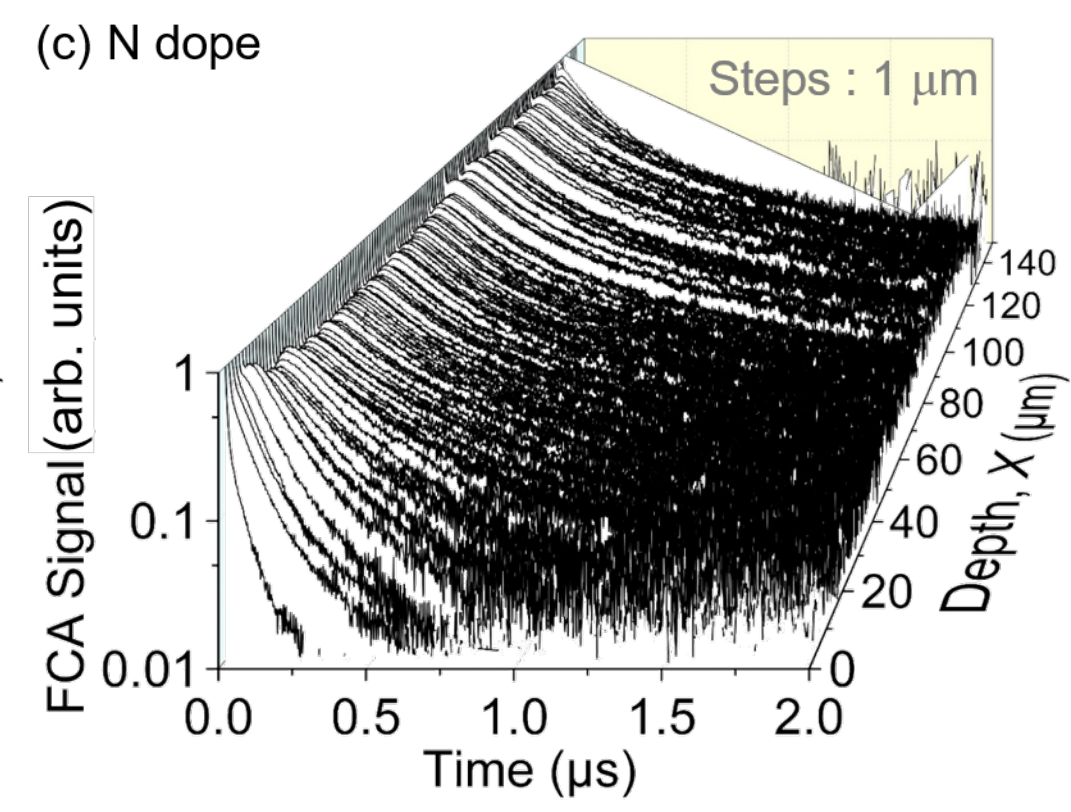
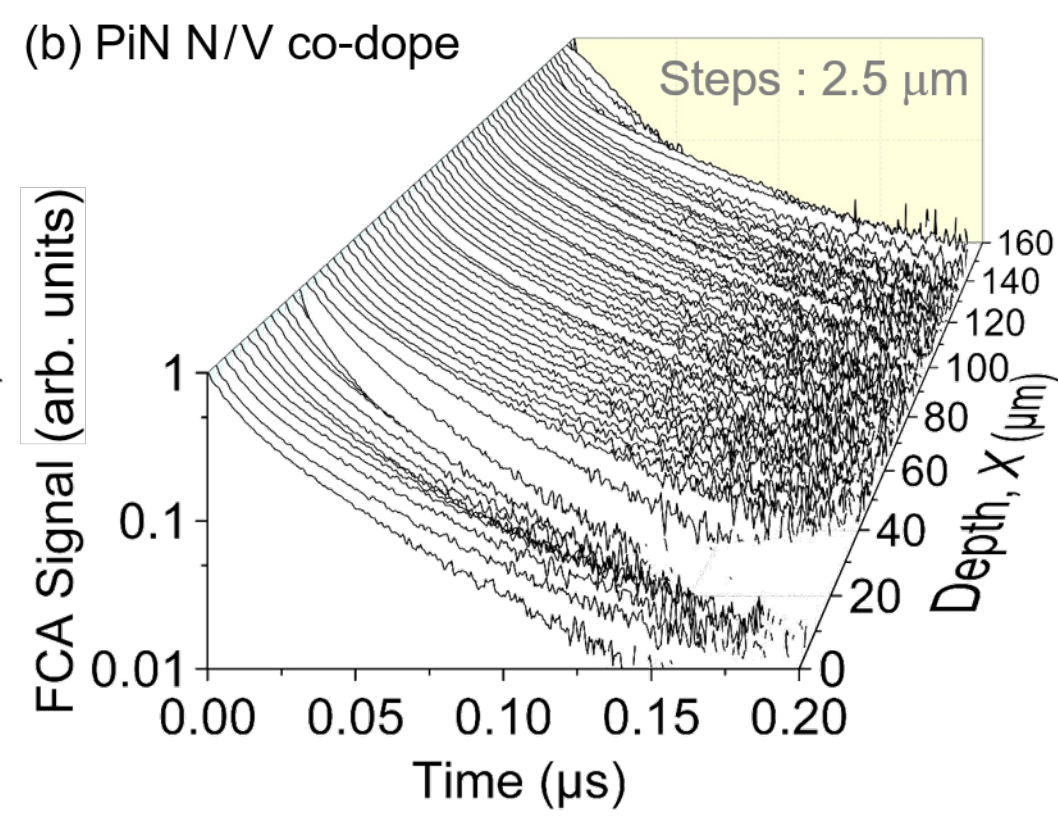
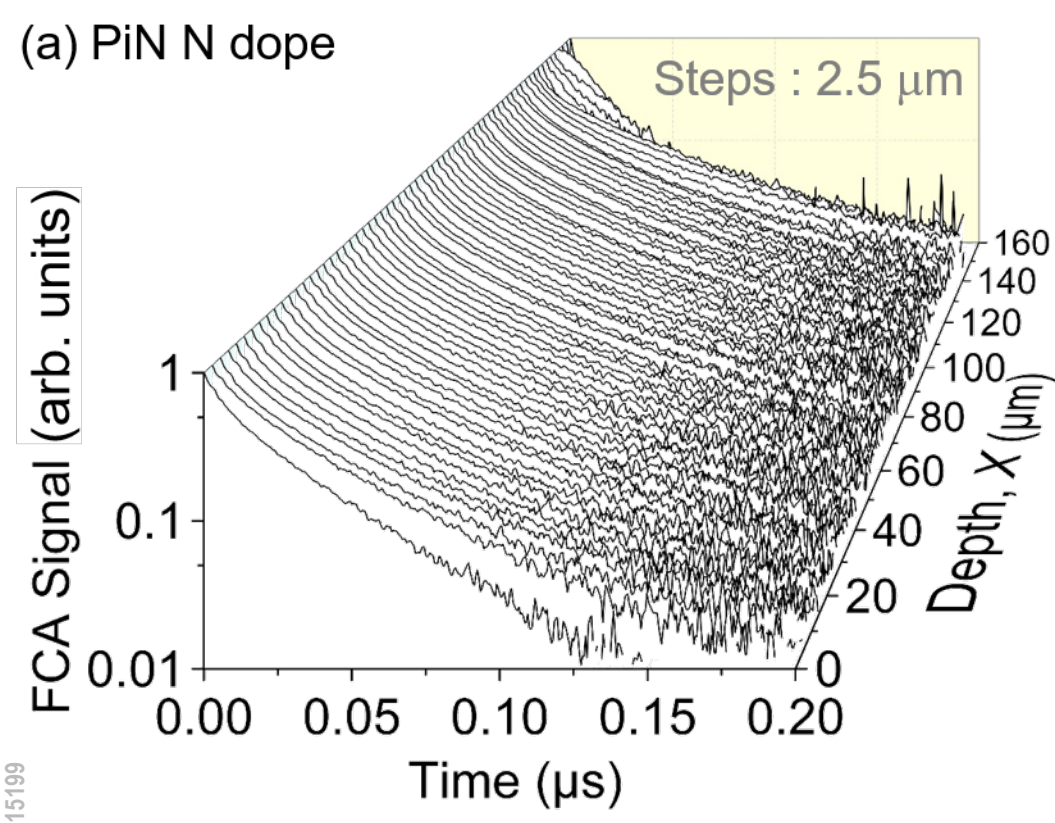
(a) Fine measurement



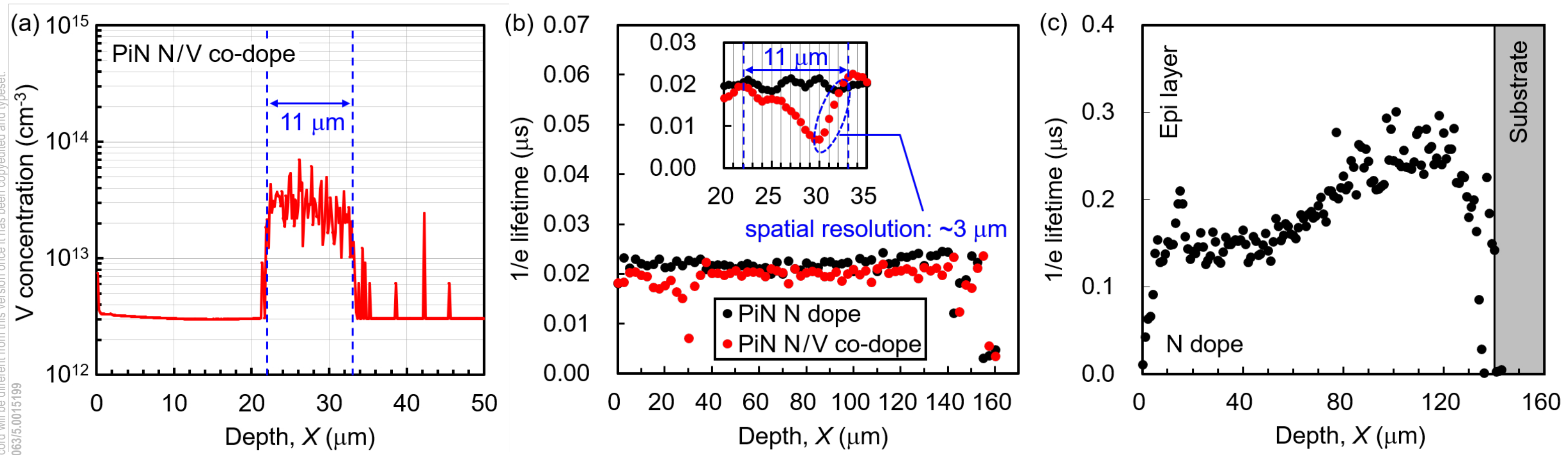
(b) Expanded measurement



This is the author's peer reviewed, accepted manuscript. However, the online version of record will be different from this version once it has been copyedited and typeset.
PLEASE CITE THIS ARTICLE AS DOI: 10.1063/5.0015199

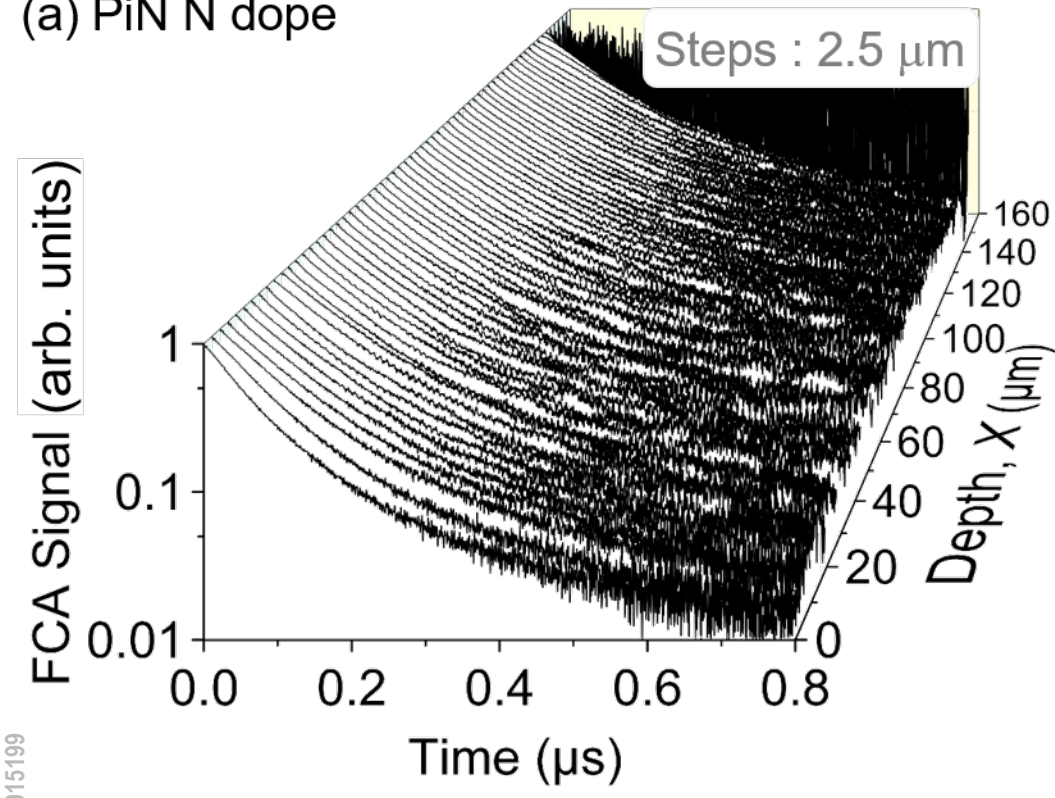


This is the author's peer reviewed, accepted manuscript. However, the online version of record will be different from this version once it has been copyedited and typeset. PLEASE CITE THIS ARTICLE AS DOI: 10.1063/5.0015199

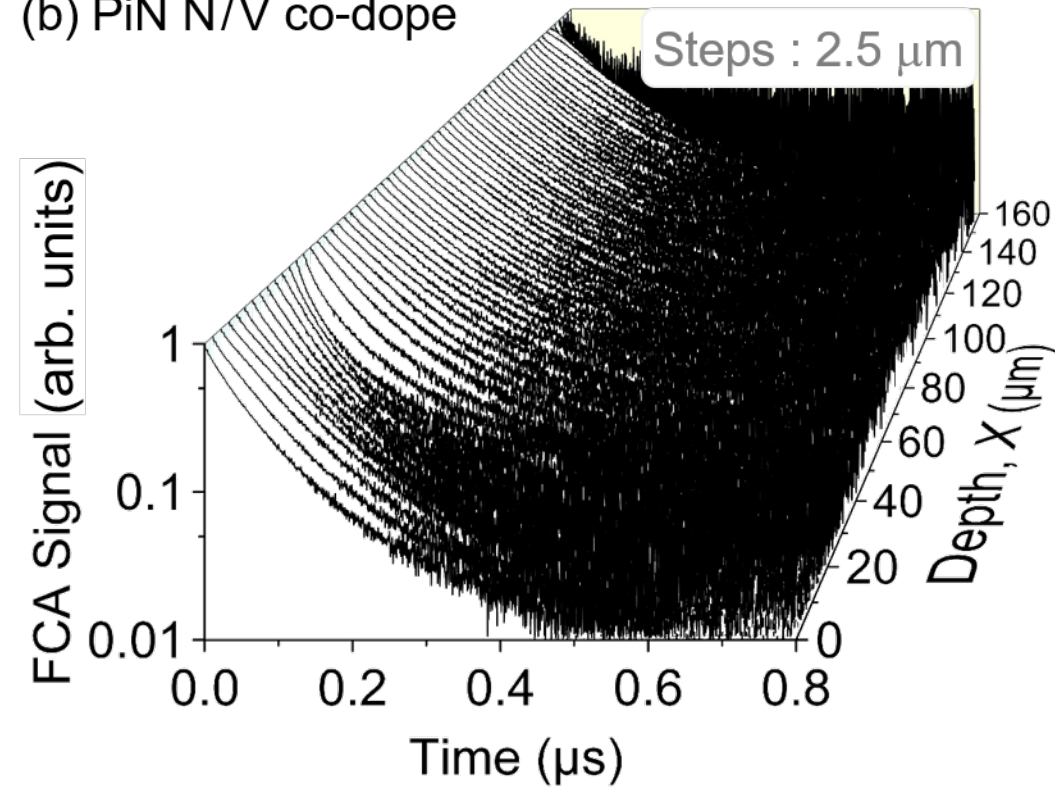


This is the author's peer reviewed, accepted manuscript. However, the online version of record will be different from this version once it has been copyedited and typeset.
PLEASE CITE THIS ARTICLE AS DOI: 10.1063/5.0015199

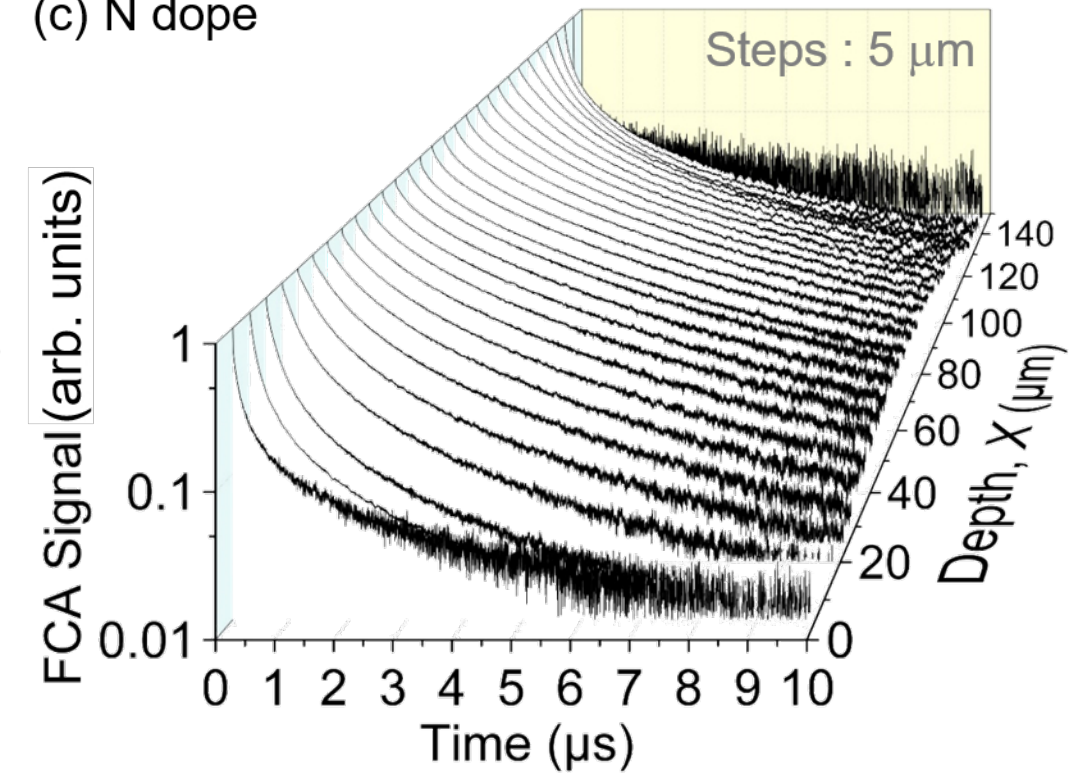
(a) PiN N dope



(b) PiN N/V co-dope



(c) N dope



This is the author's peer reviewed, accepted manuscript. However, the online version of record will be different from this version once it has been copyedited and typeset.
PLEASE CITE THIS ARTICLE AS DOI: 10.1063/5.0015199

